

# Monte Carlo renormalization group study of the Heisenberg and the XY antiferromagnet on the stacked triangular lattice and the chiral $\phi^4$ model

M. Itakura

*JSPS, Center for Promotion of Computational Science and Engineering, Japan Atomic Energy Research Institute, Taito-ku, Higashiueno 6-9-3, Tokyo 110-0015, Japan*

(November 5, 2018)

With the help of the improved Monte Carlo renormalization-group scheme, we numerically investigate the renormalization group flow of the antiferromagnetic Heisenberg and XY spin model on the stacked triangular lattice (STA-model) and its effective Hamiltonian,  $2N$ -component chiral  $\phi^4$  model which is used in the field-theoretical studies. We find that the XY-STA model with lattice size  $126 \times 144 \times 126$  exhibits clear first-order behavior. We also find that the renormalization-group flow of the STA model is well reproduced by the chiral  $\phi^4$  model, and that there are no chiral fixed points of renormalization-group flow for  $N = 2$  and 3 cases. This result indicates that the Heisenberg-STA model also undergoes first-order transition.

PACS numbers: 75.10.Nr

## I. INTRODUCTION

The critical behavior of the antiferromagnetic vector spin models on the stacked triangular lattice (STA) is still a controversial issue even after twenty years of extensive studies by means of experimental, field-theoretical, and numerical methods. See<sup>1,2,3,4</sup> for recent works, and<sup>5</sup> for a review.

The field-theoretical renormalization group (RG) analysis tells that when the number of spin component  $N$  is greater than some threshold value  $N_c$ , there are so-called "chiral fixed points" of the RG which control the critical behavior and are characterized by novel values of critical exponents, while for  $N < N_c$  such fixed points disappear and the phase transition is of first order (see<sup>5</sup> for a review). Theoretical estimations of  $N_c$  have been made by various authors by means of  $\epsilon$ -expansion<sup>2,6,7</sup>, fixed dimensional perturbation<sup>2,8</sup>, local potential approximation<sup>9</sup>, and effective average action approach<sup>1</sup>, but the estimated values range from negative value to 6.5, depending on the method employed (however, recent results tend to be around 6.0). Thus the critical behaviors of the physical relevant cases  $N = 2$  (XY spin) and  $N = 3$  (Heisenberg spin) are still unclear. A number of experimental studies<sup>3</sup> and numerical simulations<sup>10,11</sup> have yielded results which suggest second-order phase transition for  $N = 2$  and 3. However, recently it has been pointed out that the critical exponent  $\eta$ , calculated from the scaling relation, becomes negative in some of these results, which is unphysical and indicates that the observed critical behavior is in fact pseudo-critical behavior induced by the slow RG flow<sup>1,4,9</sup>.

The present work intends to clarify the issue by numerically observing the RG flow and investigating whether there are chiral fixed points or not for several values of  $N$ . The paper is

organized as follows: in the next section, we will present the method by which we observe the RG flow in the Monte Carlo simulations. Details of the Monte Carlo simulations are given in Sec. III. In Sec. IV the RG flow diagrams obtained from the simulations for  $N = 2, 3, 8$  cases are presented. The last section is devoted to the concluding remarks.

## II. NUMERICAL OBSERVATION OF THE RG FLOW

### A. chiral $\phi^4$ model

The critical behavior of the  $N$ -component STA model is essentially described by the following  $2N$ -component Ginzburg-Landau-Wilson Hamiltonian<sup>5</sup>:

$$H = \int dx \left[ K \left( (\nabla \vec{\phi}_a)^2 + (\nabla \vec{\phi}_b)^2 \right) + r \left( \vec{\phi}_a^2 + \vec{\phi}_b^2 \right) + u \left( \vec{\phi}_a^2 + \vec{\phi}_b^2 \right)^2 + v \left( (\vec{\phi}_a \cdot \vec{\phi}_b)^2 - \vec{\phi}_a^2 \vec{\phi}_b^2 \right) \right], \quad (1)$$

where  $\vec{\phi} = (\vec{\phi}_a, \vec{\phi}_b)$  is  $N + N$ -component vector field defined on the continuum space. In the field-theoretical studies,  $K$  is fixed to unity to eliminate ambiguity of coefficients induced by a trivial rescaling of  $\phi$ , namely,  $\vec{\phi} \rightarrow c\vec{\phi}$ . In this regularization scheme,  $r$  plays a role of temperature. In the present work we concentrate on the case  $v \geq 0$ . Figure 1 depicts the renormalization group flow of the scaling variables  $r$ ,  $u$ , and  $v$ . There are some trivial fixed points, namely:

**H** : high-temperature fixed point  $(r, u, v) = (\infty, 0, 0)$ ,

**L0** : anisotropic low-temperature fixed point  $(-\infty, \infty, \infty)$ ,

**L1** : isotropic low-temperature fixed point  $(-\infty, \infty, 0)$ ,

**G** : Gaussian fixed point  $(0, 0, 0)$ .

The flow on the critical plane projected onto the  $u$ - $v$  plane is shown in Fig. 2 for (a)  $N < N_c$  and (b)  $N > N_c$  cases. When  $N > N_c$ , there are stable and unstable chiral fixed points denoted by  $C_1$  and  $C_2$ , respectively, beside the  $O(2N)$  symmetric and the Gaussian fixed points denoted by O and G, respectively. The two fixed points  $C_1$  and  $C_2$  approach as  $N$  decreases, and annihilate each other at  $N = N_c$ .

In the isotropic  $\phi^4$  models, the correction-to-scaling term (distance to the Wilson-Fisher fixed point) rapidly converges to zero as  $b^{-\omega}$ , where  $b$  is a renormalization factor and  $\omega \sim 0.8$  is the correction-to-scaling exponent. Therefore the asymptotic critical behavior can be observed in finite systems with moderate size. However, when an anisotropic quartic term is included in the Hamiltonian, it in general induces very slow RG flow along the anisotropy direction. The correction-to-scaling exponent at an anisotropic fixed point (if it exists) is usually of order 0.1 or less, and extremely large system is needed to observe asymptotic critical behavior in the simulation of finite systems. Even when there are no chiral fixed points and the RG flow eventually diverges, the RG flow in the intermediate region is very slow<sup>9</sup> and it is very hard to observe asymptotic first-order behavior. Thus, in the simulation of finite systems, it is crucial to check the convergence to the fixed point of the renormalized

quartic coupling constants  $u$  and  $v$ . Now let us consider how to observe these renormalized coupling constants in the numerical simulations. In the continuum theory, they describe the behavior of renormalized field variables  $\vec{\phi}(\mathbf{x}; l)$  defined as follows:

$$\vec{\phi}(\mathbf{x}; l) \equiv \int_{|\mathbf{k}| < 1/l} \exp(i\mathbf{k} \cdot \mathbf{x}) \vec{\phi}(\mathbf{k}) d\mathbf{k}, \quad (2)$$

where  $l$  is a cut-off length and  $\vec{\phi}(\mathbf{k})$  denotes Fourier component of the field  $\vec{\phi}$ . We denote by  $u_l$  and  $v_l$  the renormalized coupling constants of cut-off length  $l$ : the renormalization flow in Fig. 2 is a trajectory of  $u_l$  and  $v_l$  on the critical plane when  $l$  is increased. The renormalization behavior of these quantities may be well observed via their conjugate quantities, which are easier to observe in numerical simulations:

$$\langle (\vec{\phi}^2(\mathbf{x}; l))^2 \rangle, \quad (3)$$

$$\langle \vec{\phi}_a^2(\mathbf{x}; l) \vec{\phi}_b^2(\mathbf{x}; l) - (\vec{\phi}_a(\mathbf{x}; l) \cdot \vec{\phi}_b(\mathbf{x}; l))^2 \rangle. \quad (4)$$

Of course, these quantities are affected not only by  $u_l$  and  $v_l$  but also by other irrelevant scaling fields, such as coefficients of higher order terms like  $|\vec{\phi}|^6$  and  $|\vec{\phi}|^8$ . However, these irrelevant scaling fields rapidly vanishes (faster than the leading correction-to-scaling term in the isotropic model,  $\sim l^{-0.8}$ ) and their effects can be ignored after sufficient renormalization as long as  $u_l$  and  $v_l$  converge (or diverge) very slowly.

Note that the definition of the renormalized field  $\vec{\phi}(\mathbf{x}; l)$  needs scaling prefactor so that the coefficients such as  $u_l$  and  $v_l$  remain finite when  $l$  goes to infinity. The following scaling scheme is simple and suitable for numerical simulations<sup>12</sup>:

$$\vec{\phi}'(\mathbf{x}; l) \equiv \frac{\vec{\phi}(\mathbf{x}; l)}{\sqrt{\langle \vec{\phi}^2(\mathbf{x}; l)^2 \rangle}}. \quad (5)$$

Substituting  $\vec{\phi}(\mathbf{x}; l)$  by  $\vec{\phi}'(\mathbf{x}; l)$ , equation (3) and (4) lead as follows:

$$\frac{\langle (\vec{\phi}'^2(\mathbf{x}; l))^2 \rangle}{\langle (\vec{\phi}'^2(\mathbf{x}; l)) \rangle^2}, \quad (6)$$

$$\frac{\langle \vec{\phi}'_a^2(\mathbf{x}; l) \vec{\phi}'_b^2(\mathbf{x}; l) - (\vec{\phi}'_a(\mathbf{x}; l) \cdot \vec{\phi}'_b(\mathbf{x}; l))^2 \rangle}{\langle (\vec{\phi}'^2(\mathbf{x}; l)) \rangle^2}. \quad (7)$$

Basically, in the present work, we observe these quantities in the numerical simulations of finite lattice version of the Hamiltonian (1) defined as follows:

$$H = \frac{KN}{2} \sum_{\langle ij \rangle} (\vec{\phi}(i) - \vec{\phi}(j))^2 + r \sum_i \vec{\phi}(i)^2 + u \sum_i (\vec{\phi}(i)^2)^2 + v \sum_i [(\vec{\phi}_a(i) \cdot \vec{\phi}_b(i))^2 - \vec{\phi}_a(i)^2 \vec{\phi}_b(i)^2], \quad (8)$$

where  $\vec{\phi}(i) = (\vec{\phi}_a(i), \vec{\phi}_b(i))$  is an  $N + N$ -component vector defined on the lattice site  $i$  of an  $L \times L \times L$  cubic lattice with periodic boundary condition being imposed, the summation

$\sum_{\langle ij \rangle}$  runs over all nearest neighbor pairs of the lattice site. We use a restriction  $u + v/4 - 2r = 0$  so that the minimum of the Hamiltonian takes place at  $|\vec{\phi}(i)| = 1$  to eliminate the ambiguity of the trivial rescaling of  $\phi$ . Actually we use the following parameterization:

$$r = -2\lambda, \quad u = \lambda(1 + A), \quad v = 4\lambda A \quad (9)$$

where  $A$  controls the strength of the anisotropy and  $\lambda$  controls the "hardness" of the spin—the larger  $\lambda$  is, the smaller the fluctuation of  $|\vec{\phi}(i)|$  is. A line  $\lambda = 0$  corresponds to  $u - v/4 = 0$ , on which instability of the Hamiltonian (8) occurs; thus  $\lambda$  should be positive.

In the lattice models, renormalized field corresponds to block spin variables. For example, consider a block spin variable  $\vec{\phi}_{b,L}$  defined on a block of  $b \times b \times b$  spins in an  $L \times L \times L$  lattice model. One can calculate the quantities (6) and (7) using  $\vec{\phi}_{b,L}$ , which we denote by  $U_{b,L}$  and  $V_{b,L}$ , respectively, and check the convergence or divergence of the renormalization flow. In the conventional MCRG scheme<sup>13</sup>, one calculates (6) and (7) for fixed value of  $L$  and increasing value of  $b$ . Note that, after the "renormalization" by the block spin transformation, the number of spins,  $(L/b)^3$ , decreases and the Hamiltonian does not stay in the same Hamiltonian space, unlike the continuum case. Therefore the number of block spins must be sufficiently large, i.e.  $L/b \gg 1$ , so that (6) and (7) take the same value at the fixed point for different values of  $b$ .

The present author proposed another scheme<sup>14</sup>, in which the ratio  $L/b$  is fixed and both  $L$  and  $b$  are increased. Let us denote a renormalized Hamiltonian which contains  $l^3$  block spins by  $H_l(K, r, u, v, \{w_i\})$ , where  $K, r, u, v$  are the renormalized coefficients of terms which correspond to that in the original Hamiltonian (8), and  $\{w_i\}$  denote set of coefficients of higher order irrelevant terms such as  $|\vec{\phi}|^6$ , which is not included in the original Hamiltonian. Now consider the behavior of  $\vec{\phi}_{L,L}$  and  $\vec{\phi}_{2L,2L}$ : the behavior of both quantities are described by a renormalized Hamiltonian which contains only 1 spin, but with different coefficients. Here,  $\vec{\phi}_{2L,2L}$  is a renormalized spin, obtained by applying real-space renormalization of factor- $2L$  to the original spins. Let us regard this factor- $2L$  renormalization as two successive renormalizations, namely factor-2 renormalization at first and then factor- $L$  renormalization. Accordingly, the original Hamiltonian  $H_{2L}(K, r, u, v, \{0\})$  is at first renormalized to  $H_L(K', r', u', v', \{w_i\})$ , then again renormalized to  $H_1(K'', r'', u'', v'', \{w'_i\})$ . If the starting Hamiltonian is at a fixed point and  $L$  is sufficiently large, coefficients before and after the factor-2 renormalization should remain unchanged except for the higher order coefficients  $\{w'_i\}$ <sup>15</sup>. At this stage,  $U_{2L,2L}$  and  $V_{2L,2L}$  can be calculated (in other words, factor- $L$  renormalization) from  $H_L(K', r', u', v', \{w_i\})$ , while  $U_{L,L}$  and  $V_{L,L}$  are calculated from  $H_L(K, r, u, v, \{0\})$ . Since the coefficients of these two Hamiltonians are the same (except the irrelevant ones),  $U_{2L,2L} = U_{L,L} + O(L^{-\omega})$  and  $V_{2L,2L} = V_{L,L} + O(L^{-\omega})$  should be satisfied, where  $\omega$  denotes correction-to-scaling exponent of the higher order terms such as  $|\vec{\phi}|^6$ . The so-called "phenomenological renormalization group method"<sup>16</sup> uses this property to locate the critical point.

When the Hamiltonian is not at a fixed point, the coefficients before and after the first factor-2 renormalization differ: they moves along the renormalization flow. This difference is reflected by  $U_{L,L}$  and  $V_{L,L}$ ; If the renormalization flow slowly converges to some fixed point,  $U_{L,L}$  and  $V_{L,L}$  slowly converge to some fixed value, while when the phase transition is of first-order and the renormalization flow diverges, so do  $U_{L,L}$  and  $V_{L,L}$ <sup>17</sup>. We will henceforth denote

these quantities simply by  $U_L$  and  $V_L$ , and investigate their behavior at the critical point when  $L$  is increased. Here their explicit form is written down for the readers' convenience:

$$U_L = \frac{\langle (\vec{M}^2)^2 \rangle}{\langle \vec{M}^2 \rangle^2}, \quad (10)$$

$$V_L = \frac{\langle \vec{M}_a^2 \vec{M}_b^2 - (\vec{M}_a \cdot \vec{M}_b)^2 \rangle}{\langle \vec{M}^2 \rangle^2}, \quad (11)$$

where  $\vec{M} = (\vec{M}_a, \vec{M}_b) = \sum_i \vec{\phi}(i)$ . In the past numerical studies in which only a specific model was investigated, the only way to reach the final fixed point (if it exists) or to observe asymptotic first-order behavior was to simulate extremely large systems, and it was impossible in general. In the present work, we investigate various Hamiltonians and scan the Hamiltonian space in search of fixed points. This method allows us to determine the asymptotic critical behavior by simulations of moderately large systems.

Note that, in the theoretical works one can concentrate on the RG flow on the critical plane on which inverse susceptibility vanishes, while in the numerical works one must determine the critical point from the numerical data. For this purpose we use a quantity which corresponds to the following quantity in the continuum theory:

$$\frac{\langle \int_{|k|<1/l} (\mathbf{k}/l)^2 \vec{\phi}^2(\mathbf{k}) d^D \mathbf{k} \rangle}{\langle (\vec{\phi}^2(\mathbf{x}; l)) \rangle} = l^2 \frac{\langle (\nabla \vec{\phi}(\mathbf{x}; l))^2 \rangle}{\langle (\vec{\phi}^2(\mathbf{x}; l)) \rangle}. \quad (12)$$

In the lattice models, the above quantity corresponds to the normalized correlation between two adjacent block spins. Actually we observe the following quantity:

$$C_L = \frac{\langle \vec{\phi}(\mathbf{k}_1) \cdot \vec{\phi}(-\mathbf{k}_1) \rangle}{\langle \vec{M}^2 \rangle}, \quad (13)$$

where  $\vec{\phi}(\mathbf{k}_1) = \sum_{\mathbf{r}} \vec{\phi}(r) \exp(i\mathbf{k}_1 \cdot \mathbf{r})$  with  $\mathbf{k}_1 = (2\pi/L, 0, 0)$ .

Figure 3 depicts the RG flow in  $U_L$ - $V_L$ - $C_L$  space: a number of trivial fixed points, namely, high-temperature fixed point  $(1 + 1/2N, \frac{(2N+1)(N-1)}{8N(N+1)}, 1)$ , isotropic low-temperature fixed point  $(1, \frac{N-1}{4(N+1)}, 0)$ , and anisotropic low-temperature fixed point  $(1, \frac{1}{4}, 0)$  are denoted by H,  $L_0$ , and  $L_1$ , respectively. Beside these points, there are some trivial manifolds: when the probability distribution of the order parameter  $\vec{M}$  is isotropic, a relation  $V_L = \frac{N-1}{4(N+1)} U_L$  is satisfied, while in the strong anisotropy limit where  $\vec{M}_a \cdot \vec{M}_b = 0$  and  $|\vec{M}_a| = |\vec{M}_b|$  hold,  $V_L = U_L/4$  is satisfied. At the Gaussian fixed point, the behavior of the finite system is governed by the zero-mode<sup>14</sup>, therefore the Gaussian fixed point lies on the  $C_L = 0$  plane. The RG flow on the critical plane, projected onto the  $U_L$ - $V_L$  plane, is shown in Fig. 4 for (a)  $N < N_c$  and (b)  $N > N_c$  cases. In both cases, the RG flow along the (approximately) horizontal direction rapidly converges, while along the (approximately) vertical direction the flow is expected to slowly converge/diverge.

To obtain the RG flow on the critical plane, we investigate the Hamiltonian (8) for various values of  $A$  and  $\lambda$ , tuning  $K$  so that  $C_L = C_{2L}$  is satisfied and observe the difference

between  $(U_L, V_L)$  and  $(U_{2L}, V_{2L})$ . It should be noted that the above definition of critical plane induces systematic deviation. For example, consider the RG flow of the isotropic  $\phi^4$  model (set  $v = 0$  in (8)). The flow of  $(U_L, C_L)$  near the Wilson-Fisher fixed point is depicted in Fig. 5 (a)<sup>14</sup>. If one define the critical point by  $C_L(K) = C_{2L}(K)$ , the flow of  $U_L$  becomes the one shown in Fig. 5(b), thus the arrow tends to “overshoot” the RG fixed point. However, the direction of the flow can be correctly estimated, and the systematic error vanishes as one approaches the fixed point.

## B. STA models

We also observe the RG flow of the following STA model:

$$H = -K \sum_{\langle ij \rangle} J_{ij} \vec{S}_i \cdot \vec{S}_j, \quad (14)$$

where  $\vec{S}_i$  denotes a two-component (XY) or three-component (Heisenberg) vector spin with  $|\vec{S}_i| = 1$  defined on the lattice site  $i$  of the stacked triangular lattice. We set  $J_{ij} = -1$  (antiferromagnetic) for intra-plane nearest neighbor pairs,  $J_{ij} = 3/4$  (ferromagnetic) for inter-plane nearest neighbor pairs, and  $J_{ij} = 0$  otherwise, so that the Fourier transform of  $J_{ij}$  near the antiferromagnetic mode<sup>18</sup>  $\vec{k}_{AF} = (2\pi/3, 0, 0)$  becomes isotropic in the  $\vec{k}$ -space, i.e.  $J(\vec{k}_{AF} + \vec{k}) \sim J(\vec{k}_{AF}) + c|\vec{k}|^2 + O(|\vec{k}|^4)$ . Note that the critical values of quantities such as  $U_L, V_L$ , and  $C_L$  do not depend on the microscopic lattice structure, but *do* depend on the macroscopic lattice structure such as boundary conditions and aspect ratios<sup>19,20</sup>. Therefore we use rectangular system which contains  $L_x \times L_y \times L_z$  spins (see Fig. 6), imposing periodic boundary condition for all three directions. The aspect ratio then becomes  $L_x : \sqrt{3}L_y/2 : L_z$ . We simulate the system with  $(L_x, L_y, L_z) = (21, 24, 21), (42, 48, 42), (84, 96, 84)$ , and  $(126, 144, 126)$ , all of which give aspect ratio  $1 : 0.99 \dots : 1$ .

The order parameter is defined as follows<sup>5</sup>:

$$\vec{M}_a = \text{Re}[\vec{S}(\vec{k}_{AF})] = \vec{M}_A - \frac{1}{2}\vec{M}_B - \frac{1}{2}\vec{M}_C, \quad (15)$$

$$\vec{M}_b = \text{Im}[\vec{S}(\vec{k}_{AF})] = \frac{\sqrt{3}}{2}\vec{M}_B - \frac{\sqrt{3}}{2}\vec{M}_C, \quad (16)$$

where  $\vec{S}(\vec{k}_{AF})$  denotes Fourier component of  $\vec{S}_i$  at  $\vec{k}_{AF}$ , and  $\vec{M}_A, \vec{M}_B, \vec{M}_C$  denote the magnetization on the three sublattices. Then  $U_L$  and  $V_L$  are calculated from Eq. (10) and Eq. (11).  $C_L$  is calculated as follows:

$$C_L = \frac{\langle |\vec{S}(\vec{k}_{AF} + \vec{k}_1)|^2 + |\vec{S}(\vec{k}_{AF} - \vec{k}_1)|^2 \rangle}{\langle \vec{S}^2(0) \rangle}, \quad (17)$$

where  $\vec{k}_1$  is the smallest, non-zero momentum in the  $\vec{k}$ -space. We observed the values of  $C_L$  for three kinds of direction, namely,  $\vec{k}_1 = (\frac{2\pi}{L_x}, 0, 0), (0, \frac{4\pi}{\sqrt{3}L_y}, 0)$ , and  $(0, 0, \frac{2\pi}{L_z})$ , and confirmed that they coincide each other within statistical errors. This indicates that the simulated system is spatially isotropic.

### III. MONTE CARLO SIMULATION

#### A. chiral $\phi^4$ models

We used the usual single-spin update Metropolis algorithm, since there is no spin reflection axis which preserves the anisotropy term in (8) and the cluster algorithm<sup>21</sup> cannot be applied. In a single-spin update process, the new spin value was chosen as follows:

$$\vec{\phi}_{new}(i) = \vec{\phi}_{old}(i) + \frac{R_g}{\sqrt{2N}} \vec{G} \quad (18)$$

where  $\vec{G}$  is an  $2N$ -component vector whose components are independent Gaussian random variables with average 0 and variance 1. The optimum value of the amplitude of random move,  $R_g$ , was determined by simulating small systems. The optimum value was found to be  $R_g \approx 0.3$  for all  $N$ ,  $A$ , and  $\lambda$ . Each Metropolis sweep was followed by one overrelaxation-type update<sup>22</sup>. Hereafter we refer one Metropolis sweep plus one overrelaxation-type sweep as ‘‘MCS’’.

Physical quantities were observed for every  $C_{INT} \times L^2$  MCS, where  $C_{INT}$  is a constant which is adjusted so that the correlations between successively observed quantities become less than 0.70, namely:

$$\frac{\langle X_t X_{t+1} \rangle - \langle X_t \rangle^2}{\langle X_t^2 \rangle - \langle X_t \rangle^2} < 0.7, \quad (19)$$

where  $X_t$  denotes observed value of a physical quantity  $X$  at the  $t$ th observation. The value of  $C_{INT}$  varies from 0.1 to 2.0, depending mainly on  $A$ . Actual values will be summarized in the later sections. For each values of  $L$ ,  $N$ ,  $A$ , and  $\lambda$ , physical quantities were observed  $10^4$  to  $10^5$  times, depending on the accuracy required to observe the RG flow. Statistical errors were estimated by the Jackknife method. Histogram method<sup>23</sup> was used to calculate thermal averages at  $K$  slightly away from that where the simulation is actually carried out.

Simulations were mainly carried out on Fujitsu VPP5000 vector processors at JAERI. The checkerboard-wise decomposition of the lattice was used for vectorization. Furthermore, we simultaneously simulated a number of independent systems, whose spins were stored into one long vector. This promoted the vectorization, especially when  $L$  is small, and accelerated the calculations. For  $N = 8$  and  $L = 16$  system, one MCS took 0.84 ms on the VPP5000.

#### B. STA models

In the frustrated spin models, the cluster update algorithm tends to flip all the spins and does not accelerate the simulation. Therefore we again used only the single-spin update Metropolis algorithm, followed by an overrelaxation sweep, i.e. 180 degree rotation of a spin  $\vec{S}_i$  with respect to its local field  $\sum_j J_{ij} \vec{S}_j$ . In the Metropolis update, the new spin direction was chosen as follows:

$$S_x = \sqrt{1 - z^2} \cos(\theta), \quad S_y = \sqrt{1 - z^2} \sin(\theta), \quad S_z = z, \quad (20)$$

for Heisenberg case and

$$S_x = \cos(\theta), \quad S_y = \sin(\theta), \quad (21)$$

for XY case, where  $z$  and  $\theta$  are uniformly distributed random numbers in the range  $[-1, 1)$  and  $[0, 2\pi)$ , respectively. Physical quantities were observed for every  $L_x \times L_y/20$  MCS for the Heisenberg case and  $L_x \times L_y/10$  MCS for the XY case. This interval was long enough to satisfy the condition (19) as long as the energy histogram has no double-peak. Physical quantities were observed  $10^4$  times for all system sizes up to  $(L_x, L_y, L_z) = (42, 48, 42)$ .

To observe the energy histogram of the larger system, we also simulated very large systems  $(L_x, L_y, L_z) = (84, 96, 84)$  and  $(126, 144, 126)$  for the XY case. Owing to the prominent double-peak of the energy histogram, autocorrelation time was much longer than  $L_x \times L_y/10$  MCS in these sizes. We used  $4 \times 10^6$  MCS for the  $(84, 96, 84)$  case and  $7 \times 10^6$  MCS for the  $(126, 144, 126)$  case, which were 1000 times longer than the auto-correlation time. One MCS of  $N = 3$  and  $(L_x, L_y, L_z) = (84, 96, 84)$  system took 27 ms on the VPP5000.

### C. Stiefel's $V_{N,2}$ models

Stiefel's  $V_{N,2}$  model<sup>4</sup> corresponds to the Hamiltonian (8) with  $\lambda = \infty$  and  $A = \infty$ , in which restrictions  $\phi_a \cdot \phi_b = 0$ ,  $\phi_a^2 = \phi_b^2 = 1/2$  are imposed to all the spins. We also simulated this model and investigated the RG flow. In the Monte Carlo simulation, only the single-spin Metropolis update was used. We only simulated the  $V_{3,2}$  model, since the  $V_{2,2}$  model is known to exhibit strong first-order behavior<sup>4</sup>. In the Metropolis update, the new spin value was chosen as follows:

$$\vec{\phi}_a = (z, \sqrt{1-z^2} \cos \theta_1, \sqrt{1-z^2} \sin \theta_1)/\sqrt{2}, \quad (22)$$

$$\vec{\phi}_b = (\sqrt{1-z^2} \sin \theta_2, -\sin \theta_1 \cos \theta_2 - z \cos \theta_1 \sin \theta_2, \cos \theta_1 \cos \theta_2 - z \sin \theta_1 \sin \theta_2)/\sqrt{2} \quad (23)$$

where  $z$  and  $\theta_{1,2}$  are uniformly distributed random numbers in the range  $[-1, 1)$  and  $[0, 2\pi)$ , respectively. Physical quantities were observed for every  $L^2$  Metropolis sweeps. This interval was long enough to satisfy the condition (19) for all system sizes up to  $L = 48$ . Physical quantities were observed  $10^4$  times for these system sizes.

To observe the energy histogram of the larger system, we also simulated a very large system  $L = 64$  and  $L = 80$ . Like the STA-XY case, a prominent double-peak of the energy histogram emerges and autocorrelation time gets much longer than  $L^2$  MCS in these sizes. We used  $6 \times 10^6$  MCS for the  $L = 64$  case and  $2 \times 10^7$  MCS for the  $L = 80$  case, which were about 1000 times longer than the auto-correlation time. For the largest size  $L = 80$ , one Metropolis sweep took 22 ms on the VPP5000.

## IV. RESULTS

### A. XY case

Parameters  $\lambda$ ,  $A$ , and  $K$  at which simulations were carried out are summarized in Table I. Figure 7 shows the histogram of energy per spin,  $E = -\sum J_{ij} \vec{S}_i \vec{S}_j / L_x L_y L_z$  of the STA-XY model with  $(L_x, L_y, L_z) = (126, 144, 126)$  and  $(84, 96, 84)$  at  $K = 0.77262$ . It can be seen that the valley between the two peaks deepens as the system size increases. This is a



clear evidence of first-order transition. This peak does not appear when the size is smaller, therefore the double peak has not been observed in the past studies of STA-XY model in which smaller systems have been used. Note that the first-order behavior has already been observed in the Monte Carlo simulations of other models which possess the same symmetry as the STA-XY model, such as Stiefel model and restricted STA model<sup>24</sup>, and quasi-one dimensional STA model<sup>25</sup>. These models have stronger anisotropy than the STA-XY model and the first-order behavior can be observed in smaller systems.

The two peaks of the histogram correspond to ordered and disordered phases, and the energy difference between the peaks provides lower bound of the latent heat per spin  $\Delta$ . On the other hand, experimental measurement of specific heat of the STA-XY materials such as CsMnBr<sub>3</sub> or Holmium<sup>26</sup> indicates second-order transition or very weak first-order transition whose latent heat is beneath the resolution of measurements, thus the upper bound of the latent heat is given. To compare the strength of the first-order transition, an adimensional parameter  $c = \Delta/k_B T_c$  is usually used, where  $k_B$  denotes Boltzmann constant and  $T_c$  denotes the transition temperature. From Fig. 7, the upper bound of the latent heat per spin is estimated as  $\Delta > 7.8 \times 10^{-3}$  and  $c > 6.0 \times 10^{-3}$ , while Ref.<sup>26</sup> provides estimates  $c < 2.9 \times 10^{-5}$  for CsMnBr<sub>3</sub> and  $c < 2.8 \times 10^{-5}$  for Holmium. These *upper* bound of  $c$  obtained from experiments is far smaller than the *lower* bound of  $c$  obtained in the present work, thus there is an apparent contradiction between them.

Note that the value of  $c$  may depends on the strength of the easy-plane anisotropy of the spin and the ratio between inter and intra layer coupling constants. The result of Ref.<sup>25</sup> indicates that when the inter-layer coupling is much larger than the intra-layer coupling, the first-order transition becomes stronger. On the other hand, a weak easy-plane anisotropy will lead to Heisenberg-to-XY crossover which weaken the transition, since the transition is weakened as the number of spin component is increased and eventually becomes second-order. Actually, we will see in the following section that the STA-Heisenberg model does not exhibit as strong a transition as the STA-XY model. Thus the most plausible explanation of the apparent discrepancy between the experimental results and the present work may be that the finiteness of the easy-plane anisotropy in the experimental materials induces Heisenberg-to-XY crossover and the transition is weakened.

Figure 8 and 9 show the RG flow of  $(U_L, V_L)$  at the strong and weak anisotropy region, respectively, of the  $N = 2$  chiral  $\phi^4$  model. Figure 8 also shows the same plot for the STA-XY model. One can see that the STA-XY model is on the “runaway” trajectory, which is another evidence of first-order transition. It can also be seen that there are no stable fixed points other than the  $O(4)$  symmetric one. This means that any models or materials which possess the same symmetry as STA-XY model, namely  $Z_3 \times O(2)$ , exhibit first-order transition.

Fig. 10 shows the vertical velocity of the RG flow  $V_{2L} - V_L$  plotted against  $V_L$ . The plots for the two different sizes  $L = 6$  and  $L = 8$  coincide within statistical errors. This indicates that the system size is large enough to eliminate finite-size artifact of the RG flow. Thus we can safely extrapolate the asymptotic critical behavior from the finite-size RG flow. Moreover, the plots of the chiral  $\phi^4$  model and the STA-XY model are essentially the same. This means that the critical behavior of the STA-XY model is well reproduced by the chiral  $\phi^4$  model.

## B. Heisenberg case

Parameters  $\lambda$ ,  $A$ , and  $K$  at which simulations were carried out are summarized in Table II. Unlike the STA-XY case, the STA-Heisenberg model does not show the double-peak behavior within the simulated size  $(L_x, L_y, L_z) = (84, 96, 84)$ . However, the  $V_{3,2}$  model with  $L = 80$  shows a clear double-peak behavior. Figure 11 shows the histogram of energy per spin,  $E = 3 \cdot L^{-3} \sum J_{ij} (\vec{S}_i - \vec{S}_j)^2$  at  $K = 0.217685$ . Although it is necessary to simulate larger system and show that the valley between the two peaks deepens to confirm the first-order transition, this double-peak strongly indicate that the transition is of first-order.

Figure 12 and 13 show the RG flow of  $(U_L, V_L)$  at the strong and weak anisotropy region, respectively, of the  $N = 3$  chiral  $\phi^4$  model. Figure 12 also shows the same plot for the STA-Heisenberg model and the  $V_{3,2}$  model. It can be seen that the STA-Heisenberg model and the  $V_{3,2}$  model are on the “runaway” trajectory, therefore undergo first-order transition in the thermodynamic limit. It can also be seen that there are no fixed points other than the  $O(6)$  symmetric one. This means that any models or materials which possess the same symmetry as STA-Heisenberg model, namely  $Z_3 \times O(3)$ , exhibit first-order transition. From Fig. 12, we roughly estimate that  $L = 96$  STA-Heisenberg model needs factor-2 renormalizations three or more times to reach the strong first-order region, which means that the clear first-order behavior will be observed in an  $L \sim 800$  system.

Fig. 14 shows the vertical velocity of the RG flow  $V_{2L} - V_L$  plotted against  $V_L$ . In this case, this quantity depends not only on  $V_L$  but also on  $U_L$ , although the dependence is not so strong. Therefore the plot can not be fitted to a single line well. However, there is no systematic deviation between the plots of the two different sizes. Thus we can safely extrapolate the asymptotic critical behavior from the finite-size RG flow. As in the XY case, the plots of the chiral  $\phi^4$  model and the STA-Heisenberg model are essentially the same and the critical behavior of the STA-Heisenberg model is well reproduced by the chiral  $\phi^4$  model.

## C. $N = 8$ case

It is necessary to demonstrate that the MCRG scheme presented in Sec. II is able to detect the chiral fixed point if it does exist. For this purpose, we investigate  $N = 8$  case, which is greater than any theoretical estimate of  $N_c$  in literature<sup>1,2,6,7,8,9</sup>. Parameters  $\lambda$ ,  $A$ , and  $K$  at which simulations were carried out are summarized in Table III. Figure 15 shows the RG flow of  $(U_L, V_L)$  for  $L = 8 \rightarrow 16$ . The stable chiral fixed point  $C_1$  and the unstable chiral fixed point  $C_2$  are clearly seen.

Fig. 16 shows the vertical velocity of the RG flow  $V_{2L} - V_L$  plotted against  $V_L$ , using only the data near the stable fixed point  $C_1$ . Unlike the  $N = 2$  and the  $N = 3$  case, this plot has a zero. The plots of the two different size coincide within statistical error, which indicates that the simulated system is large enough to observe the RG flow.

## V. CONCLUSION

The large scale Monte Carlo simulation of the STA-XY model has revealed that the transition is of first-order. This is the first numerical work to confirm the first-order transi-

tion of the simple and isotropic STA-XY model. The result also indicate that the transition is strong enough to be observed in experiments. But the finiteness of the easy-plane spin anisotropy of the actual materials will weaken the transition compared to the STA-XY model simulated in the present work, in which the easy-plane anisotropy is infinitely strong.

We have also investigated the RG flow the  $2N$ -component chiral  $\phi^4$  model numerically and have found that there are no chiral fixed points in  $N = 2$  and  $N = 3$  cases, and we conclude that the STA-Heisenberg model also undergoes first-order transition. By a rough estimate, we expect that the STA-Heisenberg model exhibits strong first-order behavior when the size is larger than  $L = 800$ . For  $N = 8$  case, we have found the chiral fixed points, thus the value of  $N_c$  is estimated as  $3 < N_c < 8$ . Further study to determine the precise value of  $N_c$  may be of some interest, because such a study will serve to test the accuracy of field theoretical techniques. However, once the nature of physical relevant case  $N = 3$  and  $N = 2$  is clarified, the precise value of  $N_c$  is of less importance.

## VI. ACKNOWLEDGMENTS

The present author is grateful to D. Loison, B. Delamotte, K. B. Varnashev, and H. Kawamura for useful comments.

- 
- <sup>1</sup> M. Tissier, B. Delamotte, and D. Mouhanna, Phys. Rev. Lett. **84**, 5208 (2000); preprint, `cond-mat/0107183`.
- <sup>2</sup> A. Pelissetto, P. Rossi and E. Vicari Phys. Rev. B **63** R140414 (2001); Nucl. Phys. B **607**, 605 (2001); Phys. Rev. B **65** 020403 (2002).
- <sup>3</sup> V. P. Plakhty, J. Kulda, D. Visser, E. V. Moskvina, and J. Wosnitza, Phys. Rev. Lett. **85**, 3942 (2000).
- <sup>4</sup> D. Loison and K. D. Schotte, Euro. Phys. J.B **14**, 125 (2000).
- <sup>5</sup> H. Kawamura, J. Phys.: Condens. Matter **10**, 4707 (1998).
- <sup>6</sup> H. Kawamura, J. Phys. Soc. Jpn. **59**, 2305 (1990).
- <sup>7</sup> S. A. Antonenko, A. I. Sokolov and K. B. Varnashev, Phys. Lett. A **208**, 161 (1995).
- <sup>8</sup> S. A. Antonenko and A. I. Sokolov, Phys. Rev. B **49**, 15901 (1994).
- <sup>9</sup> G. Zumbach, Phys. Rev. Lett. **71**, 2421 (1993); Nucl. Phys. B **413**, 771 (1994).
- <sup>10</sup> H. Kawamura, J. Phys. Soc. Jpn. **61**, 1299 (1992).
- <sup>11</sup> M. L. Plumer and A. Mailhot, Phys. Rev. B **50**, 16113 (1994).
- <sup>12</sup> In the homogenous models with translational symmetry, the prefactor  $\langle \vec{\phi}(\mathbf{x}; l)^2 \rangle$  do not depend on the position  $\mathbf{x}$ . In the inhomogenous models such as random bond or diluted spin models, this factor should be replaced by  $[\langle \vec{\phi}(\mathbf{x}; l)^2 \rangle]$  where  $[\cdot \cdot \cdot]$  denotes average over  $\mathbf{x}$  and the randomness in the Hamiltonian.
- <sup>13</sup> R.H.Swendsen, Phys. Rev. Lett. **42**, 859 (1979).
- <sup>14</sup> M. Itakura, Phys. Rev. E **61**, 5924 (2000).
- <sup>15</sup> Alternatively, one can use this condition as a definition of the fixed point. The critical value of the relevant scaling fields do not depends on the definition.

- <sup>16</sup> K. Binder, Z. Phys. B **43**, 119 (1981).
- <sup>17</sup> For example, see M. Itakura, Phys. Rev. B **60**, 6558 (1999).
- <sup>18</sup> The first Brillouin zone is an (approximately regular) hexagon in the  $x$ - $y$  plane and  $\vec{k}_{AF}$  is on the vertex of the hexagon.
- <sup>19</sup> K. Kaneda and Y. Okabe, Phys. Rev. Lett. **86**, 2134 (2001).
- <sup>20</sup> K. Kaneda, Y. Okabe, and M. Kikuchi, J. Phys. A **32**, 7263 (1999).
- <sup>21</sup> U. Wolff, Phys. Rev. Lett. **62**, 361 (1989).
- <sup>22</sup> M. Caselle and M. Hasenbusch, J. Phys. A **31**, 4603 (1998).
- <sup>23</sup> A. M. Ferrenberg and R. H. Swendsen, Phys. Rev. Lett. **61**, 2635 (1988).
- <sup>24</sup> D. Loison and K. D. Schotte, Euro. Phys. J.B**5**, 735 (1998).
- <sup>25</sup> M. L. Plumer and A. Mailhot, J. Phys. Condens. Matter **9**, L165 (1997).
- <sup>26</sup> J. Wang, D. P. Belanger, and B. D. Gaulin, Phys. Rev. Lett. **66**, 3195 (1991).

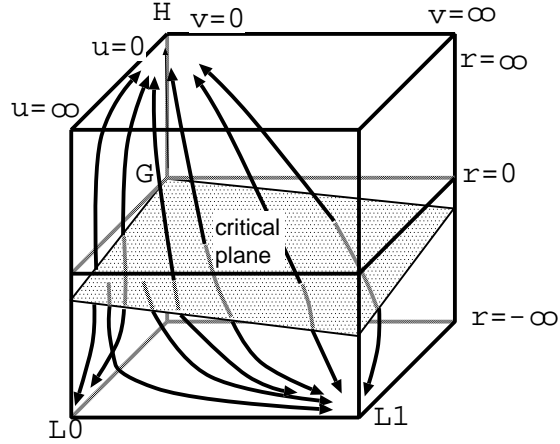


FIG. 1. Renormalization flow of  $r$ ,  $u$ , and  $v$ . H, G, L<sub>0</sub>, and L<sub>1</sub> denote the high-temperature, Gaussian, isotropic low-temperature, and anisotropic low-temperature fixed point, respectively.

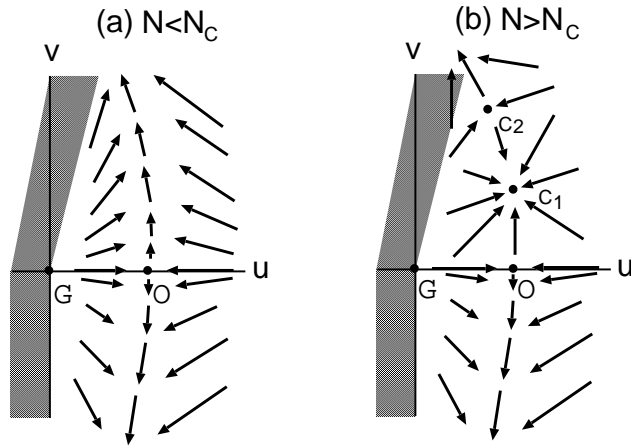


FIG. 2. Renormalization flow on the critical plane projected onto the  $u$ - $v$  plane for (a)  $N < N_c$  and (b)  $N > N_c$ . Shaded area is unstable region. G, O, C<sub>1</sub>, and C<sub>2</sub> denote Gaussian,  $O(2N)$ -isotropic, stable chiral, and unstable chiral fixed points, respectively.

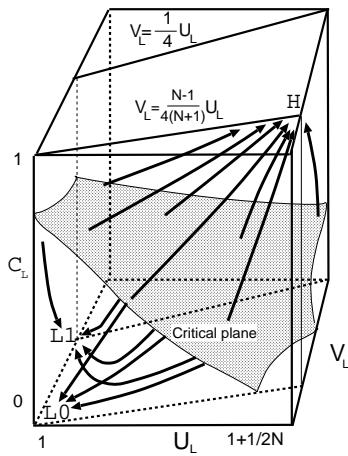


FIG. 3. Renormalization flow of  $C_L$ ,  $U_L$ , and  $V_L$ .

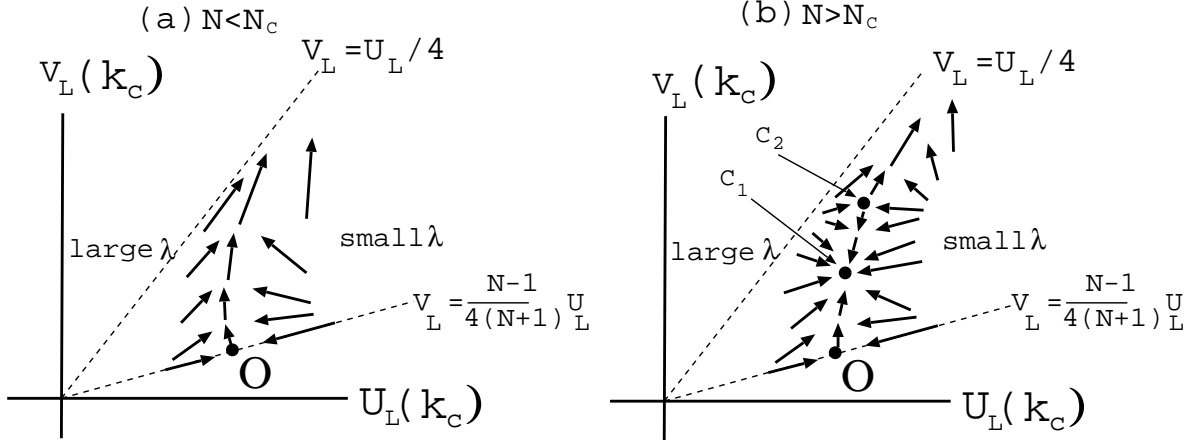


FIG. 4. Renormalization flow on the critical plane projected onto the  $U_L$ - $V_L$  plane for (a)  $N < N_c$  and (b)  $N > N_c$  cases. The symbol O,  $C_1$ , and  $C_2$  denote  $O(2N)$ -isotropic, stable chiral, and unstable chiral fixed point, respectively.

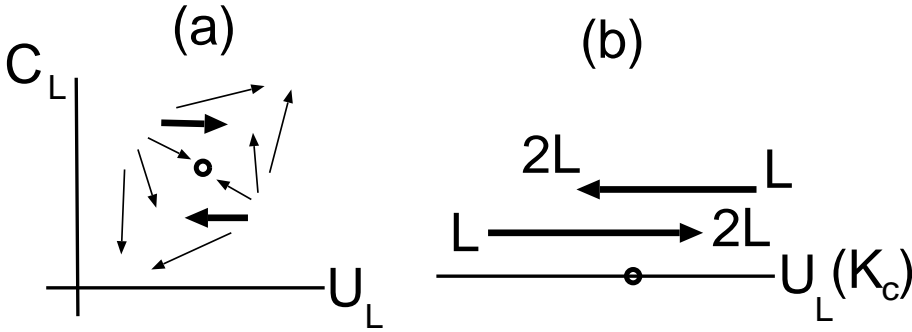


FIG. 5. (a) Renormalization flow of  $C_L$  and  $U_L$  for isotropic model  $v = 0$  near the Wilson-Fisher fixed point. (b) RG flow of  $U_L(K_c)$  tends to “overshoot” the fixed point (see the main text).

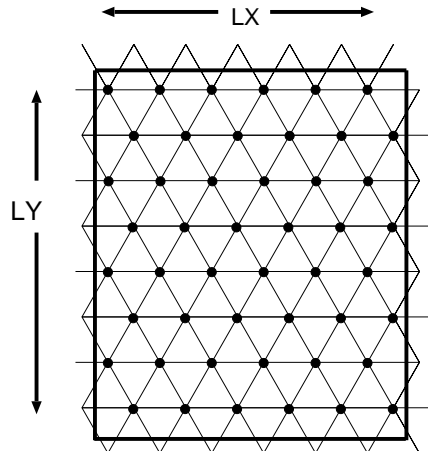


FIG. 6. Rectangular system used for the simulation of stacked triangular antiferromagnet. The figure shows a system with  $L_x = 6, L_y = 8$ . This layer is stacked  $L_z$  times.

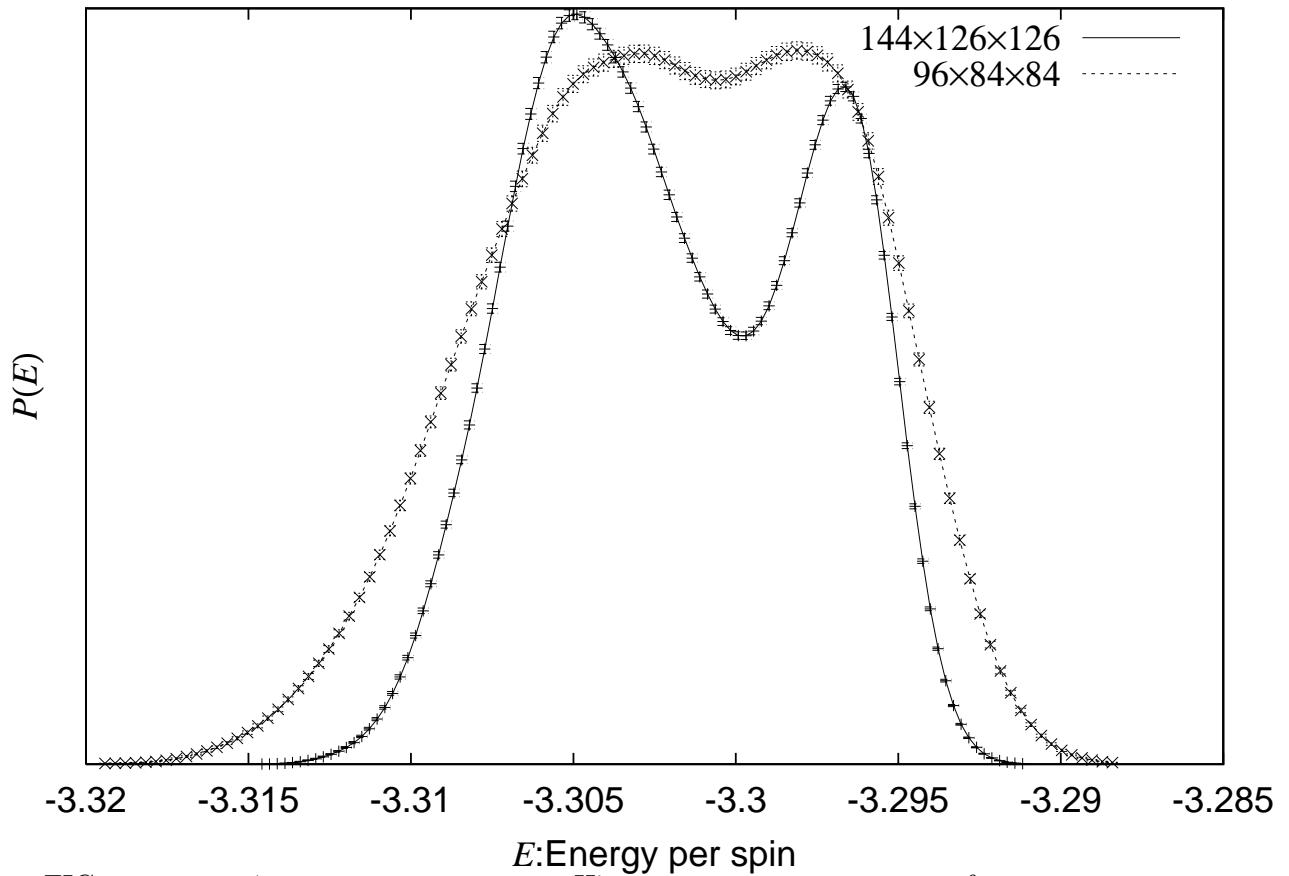


FIG. 7. Histogram of energy per spin of the STA-XY model with the size  $(L_x, L_y, L_z) = (84, 96, 84)$  and  $(126, 144, 126)$  at  $K = 0.77262$ .

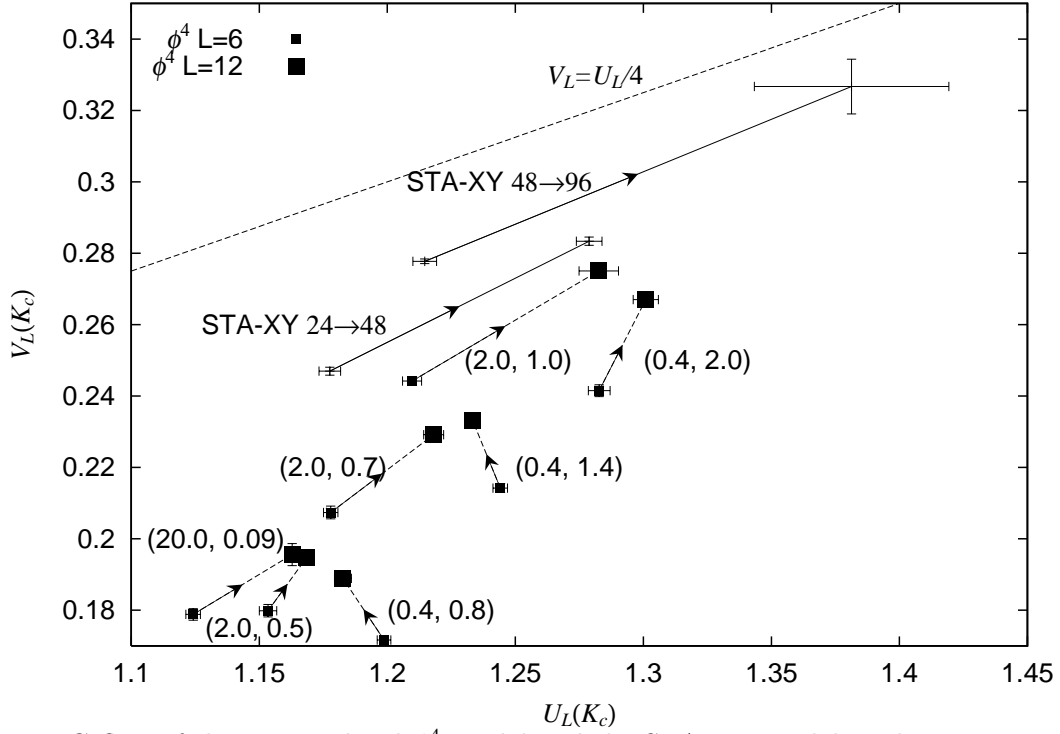


FIG. 8. RG flow of the  $N = 2$  chiral  $\phi^4$  model and the STA-XY model at the strong anisotropy region. The numbers in parenthesis are the values of  $(\lambda, A)$  of the chiral  $\phi^4$  model.

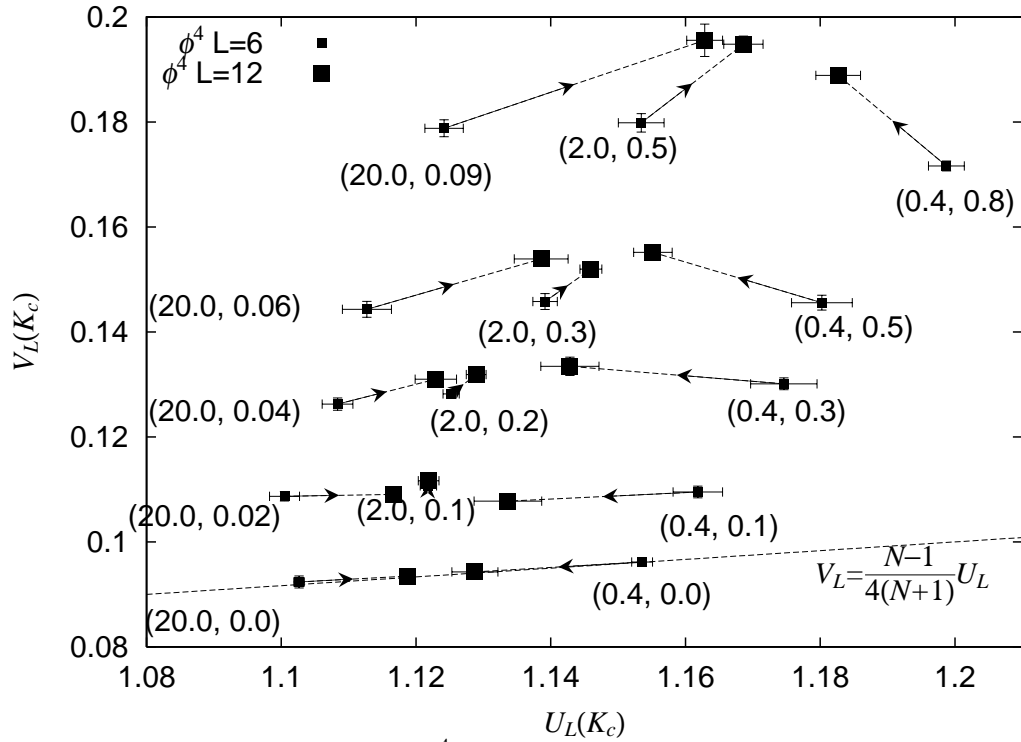


FIG. 9. RG flow of the  $N = 2$  chiral  $\phi^4$  model at the weak anisotropy region. The numbers in parenthesis are the values of  $(\lambda, A)$ .



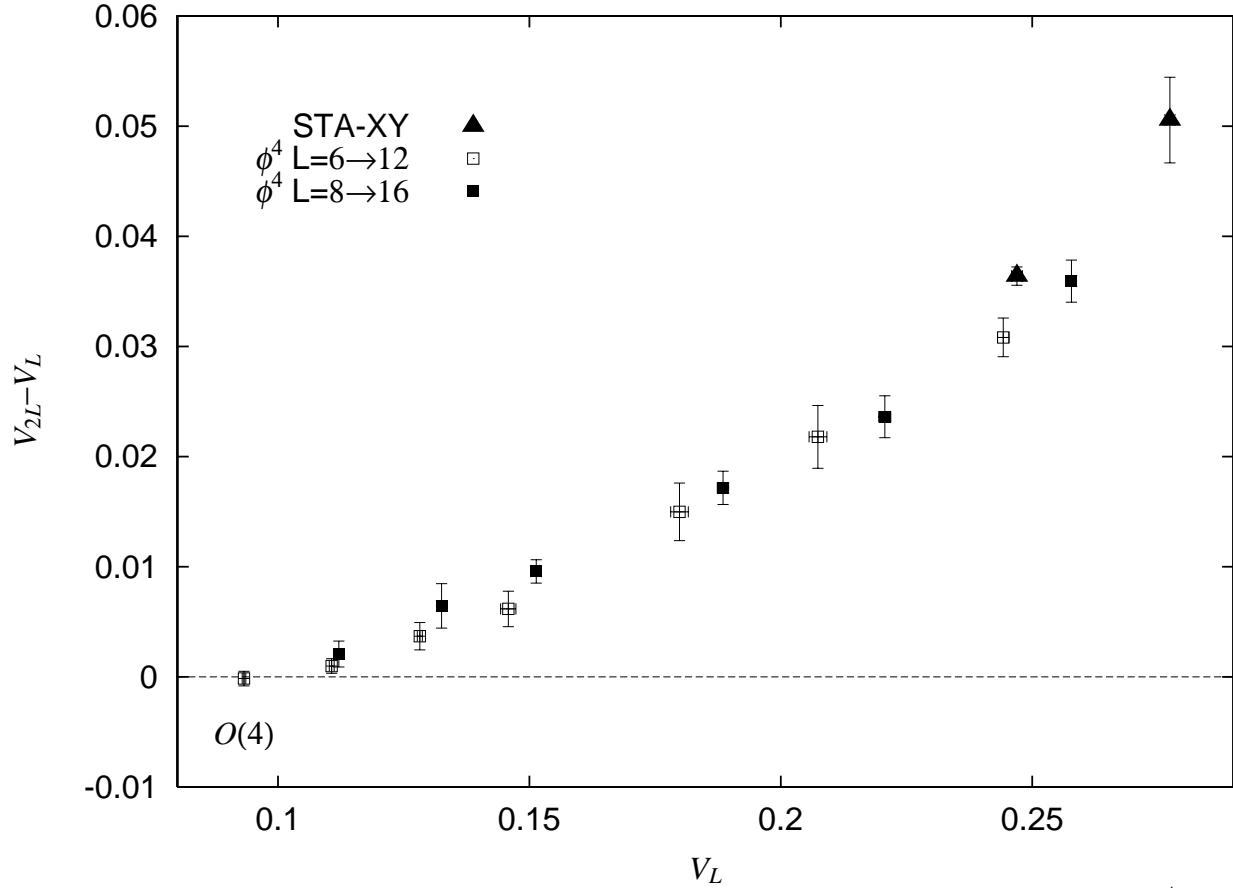


FIG. 10. The vertical velocity of the RG flow  $V_{2L} - V_L$  against  $V_L$  for the  $N = 2$  chiral  $\phi^4$  model and the STA-XY model. “ $O(4)$ ” denotes the  $O(4)$ -symmetric fixed point.

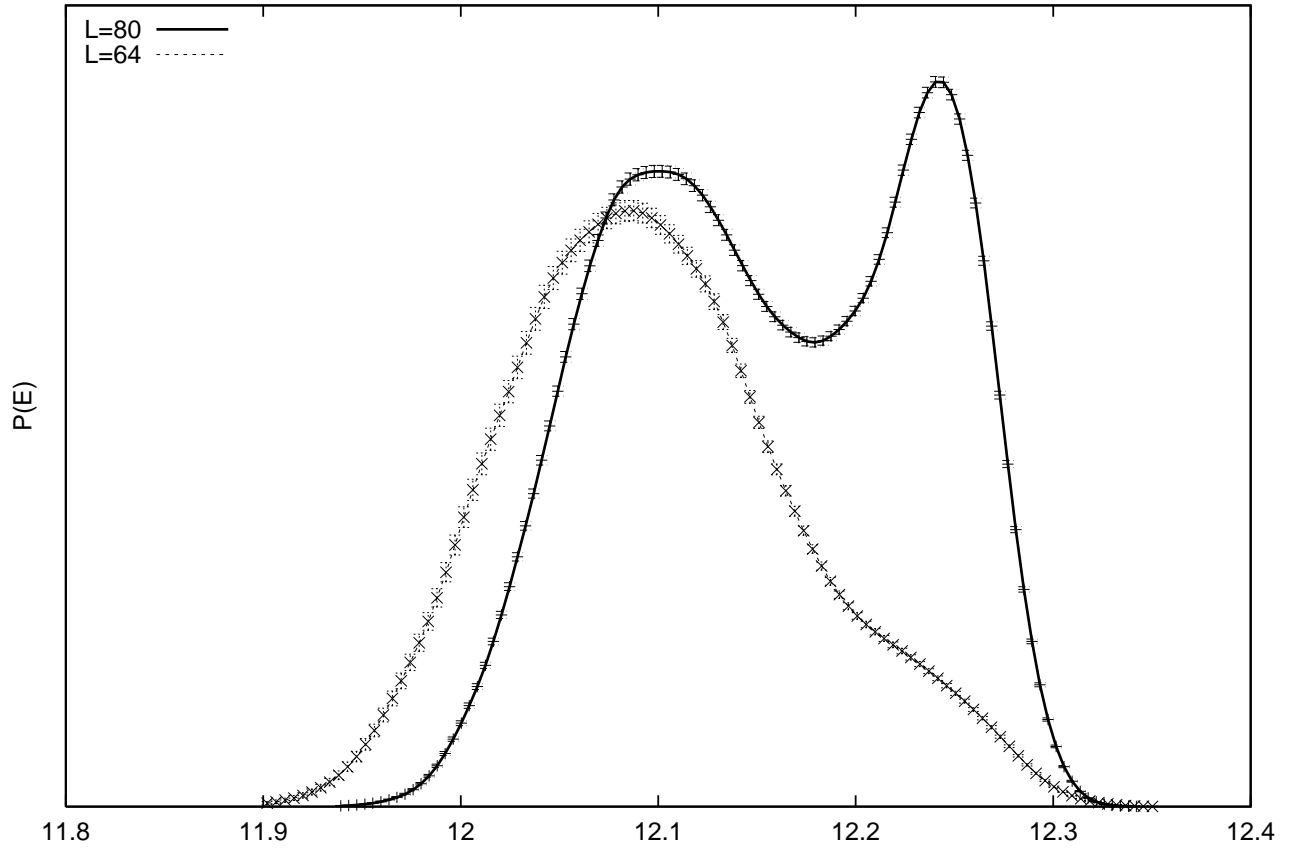


FIG. 11. Histogram of energy per spin of the  $V_{3,2}$  model with the size  $L = 64$  and  $L = 80$  at  $K = 0.217685$ .

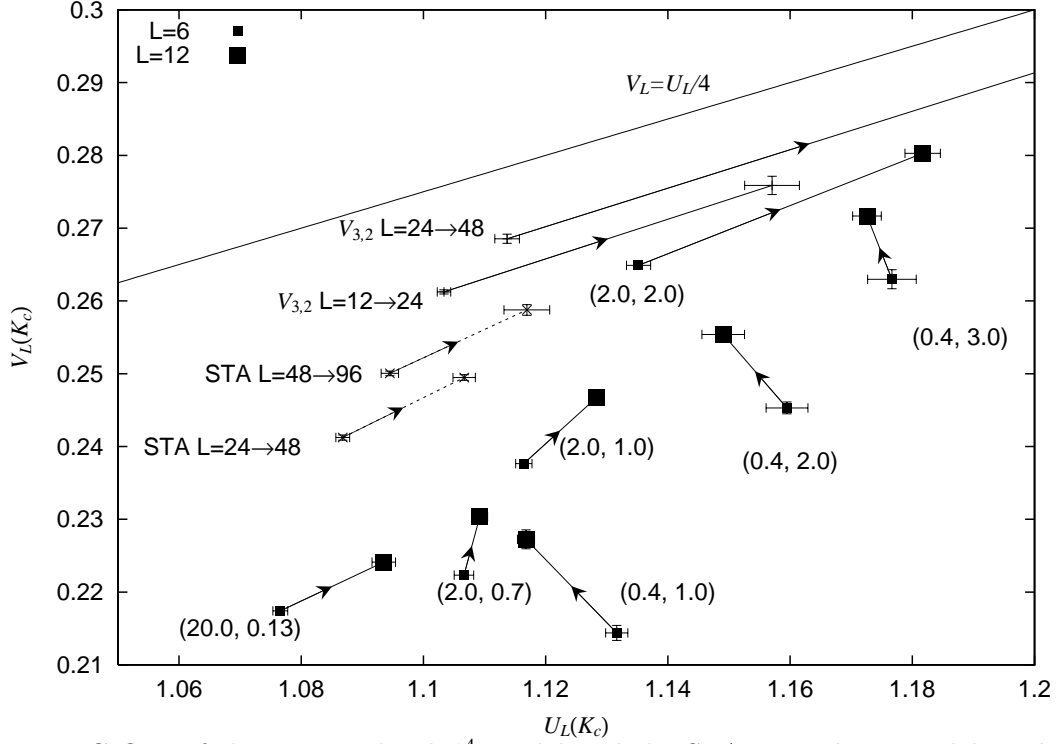


FIG. 12. RG flow of the  $N = 3$  chiral  $\phi^4$  model and the STA-Heisenberg model at the strong anisotropy region. The numbers in parenthesis are the values of  $(\lambda, A)$  of the chiral  $\phi^4$  model.

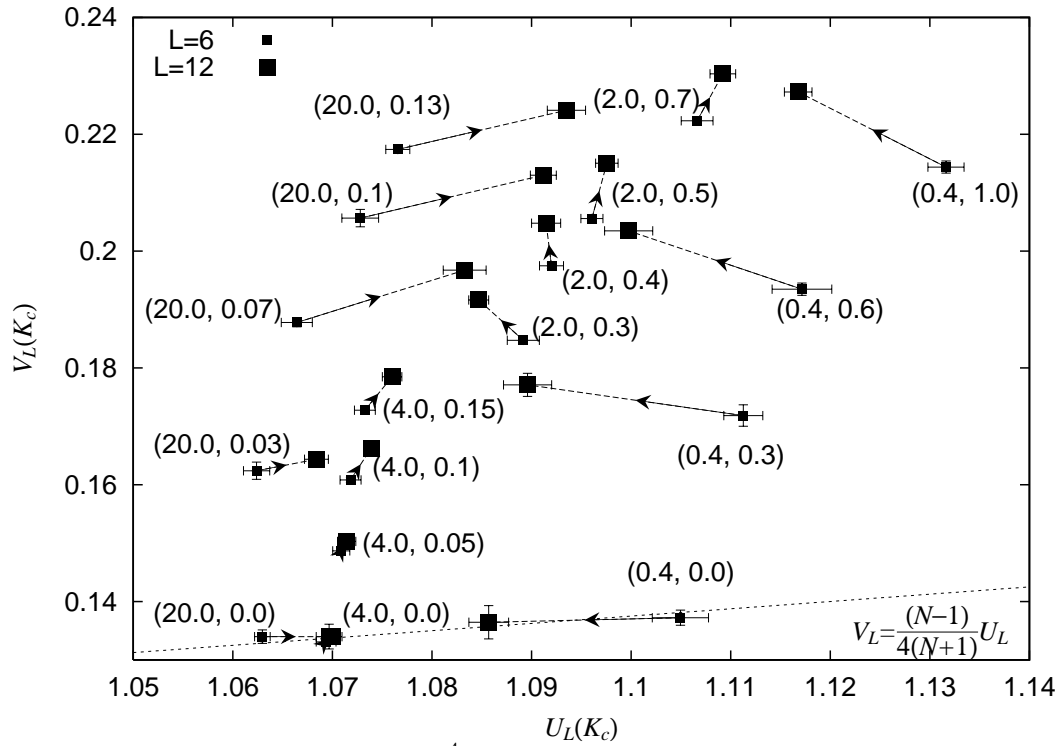


FIG. 13. RG flow of the  $N = 3$  chiral  $\phi^4$  model at the weak anisotropy region. The numbers in parenthesis are the values of  $(\lambda, A)$ .

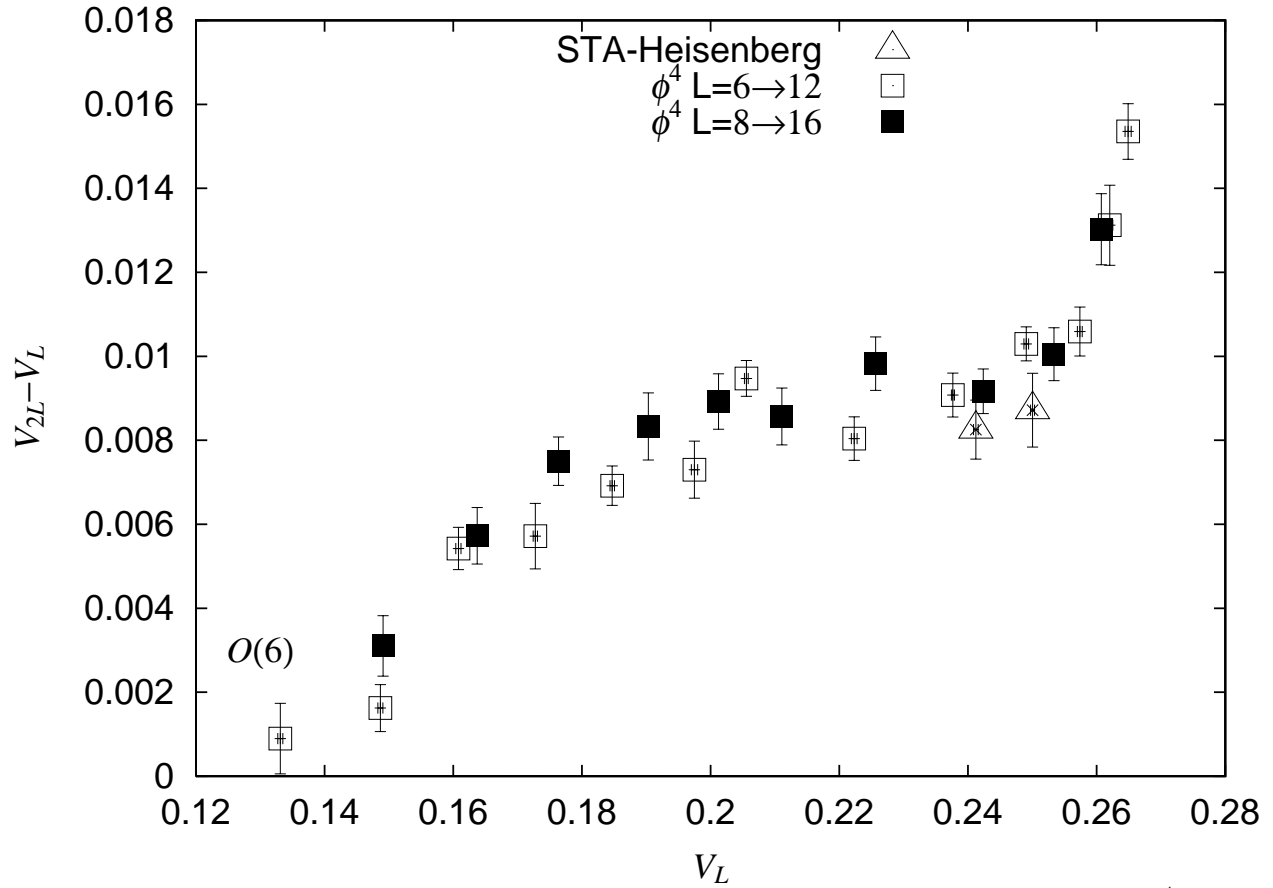


FIG. 14. The vertical velocity of the RG flow  $V_{2L} - V_L$  against  $V_L$  for the  $N = 3$  chiral  $\phi^4$  model and the STA-Heisenberg model. “ $O(6)$ ” denotes the  $O(6)$ -symmetric fixed point.

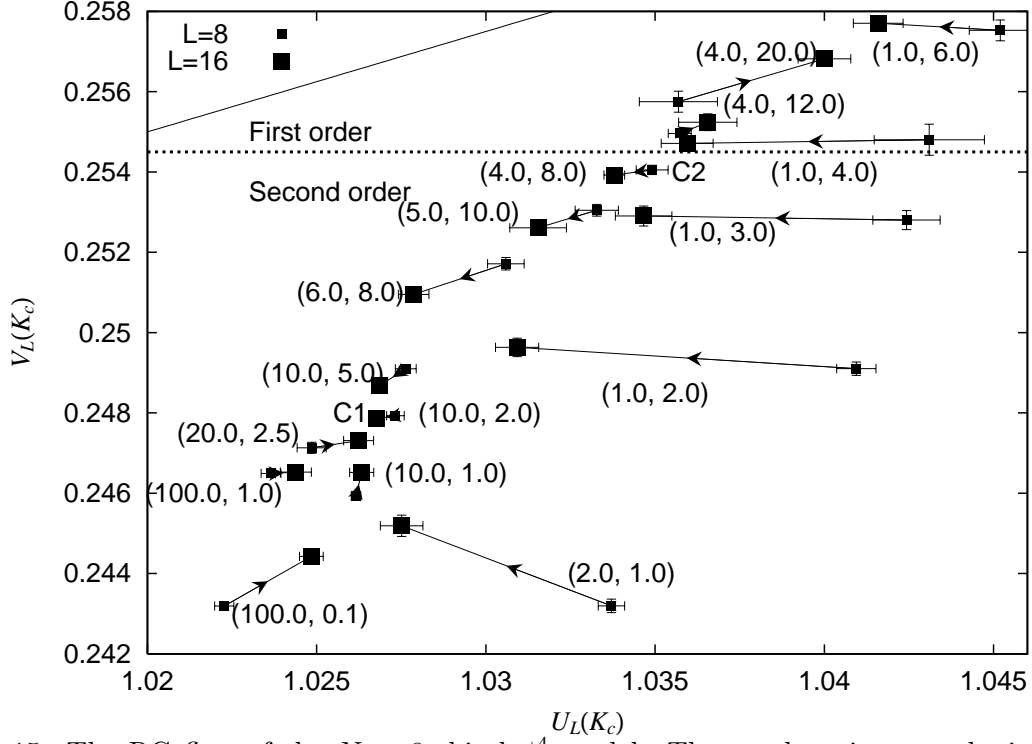


FIG. 15. The RG flow of the  $N = 8$  chiral  $\phi^4$  model. The numbers in parenthesis show the values of  $(\lambda, A)$ .  $C1$  and  $C2$  denote the stable and unstable RG fixed point, respectively.

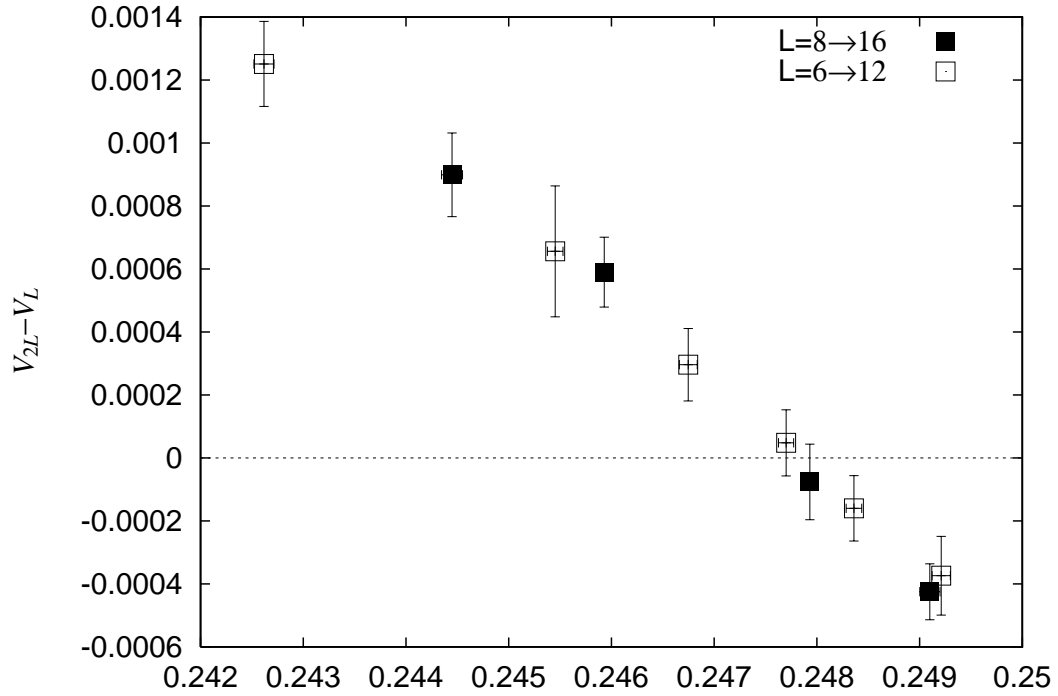


FIG. 16. The vertical velocity of the RG flow  $V_{2L} - V_L$  against  $V_L$  near the stable chiral fixed point  $C1$  of the  $N = 8$  chiral  $\phi^4$  model.

$\lambda$	$A$	$K/N$	$C_{INT}$
0.4	0.0	0.346	0.18
0.4	0.1	0.371	0.18
0.4	0.3	0.415	0.18
0.4	0.5	0.462	0.21
0.4	0.8	0.535	1.4
0.4	1.4	0.659	1.4
0.4	2.0	0.791	2.1
2.0	0.0	0.2880	0.12
2.0	0.1	0.3095	0.12
2.0	0.2	0.3292	0.12
2.0	0.3	0.3480	0.12
2.0	0.5	0.3800	0.32
2.0	0.7	0.4090	0.32
2.0	1.0	0.4510	0.40
20.0	0.00	0.2385	0.14
20.0	0.02	0.2415	0.14
20.0	0.06	0.2450	0.21
20.0	0.09	0.2460	0.35
STA		0.7726	0.10

TABLE I. Parameters  $\lambda$ ,  $A$ , and  $K$  (divided by  $N$ ) at which simulations were carried out for the  $N = 2$  chiral  $\phi^4$  model and the STA-Heisenberg model. Physical quantities were observed for every  $C_{INT} \times L^2$  MCS.

$\lambda$	$A$	$K/N$	$C_{INT}$
0.4	0.00	0.3185	0.50
0.4	0.30	0.3660	0.60
0.4	0.60	0.4130	1.2
0.4	1.00	0.4700	1.8
0.4	2.00	0.6140	1.8
0.4	3.00	0.7556	3.0
2.0	0.3	0.3218	0.14
2.0	0.4	0.3328	0.21
2.0	0.5	0.3429	0.21
2.0	0.7	0.3624	0.35
2.0	1.0	0.3890	0.35
2.0	2.0	0.4640	1.5
4.0	0.00	0.2650	0.14
4.0	0.05	0.2725	0.14
4.0	0.10	0.2776	0.14
4.0	0.15	0.2833	0.14
20.0	0.00	0.242	0.14
20.0	0.07	0.247	0.14
20.0	0.10	0.247	0.21
20.0	0.13	0.247	0.21
$V_{3,2}$		0.2176	1.0
STA		1.17286	0.05

TABLE II. Parameters  $\lambda$ ,  $A$ , and  $K$  (divided by  $N$ ) at which simulations were carried out for the  $N = 3$  chiral  $\phi^4$  model and the STA-Heisenberg model. Physical quantities were observed for every  $C_{INT} \times L^2$  MCS.

$\lambda$	$A$	$K/N$	$C_{INT}$
1.0	2.0	0.3710	0.6
1.0	3.0	0.4100	0.8
1.0	4.0	0.4505	1.6
1.0	6.0	0.5270	2.4
2.0	1.0	0.3135	0.4
4.0	5.0	0.3355	0.4
4.0	8.0	0.3475	0.8
4.0	12.0	0.3584	1.2
4.0	20.0	0.3710	2.0
5.0	10.0	0.324	0.8
6.0	5.0	0.3012	0.6
6.0	8.0	0.3044	0.7
10.0	0.6	0.2675	0.15
10.0	1.0	0.2690	0.15
10.0	1.5	0.2700	0.15
10.0	2.0	0.2710	0.4
10.0	3.0	0.2718	0.4
10.0	5.0	0.2728	0.6
20.0	2.5	0.2525	0.6
100.0	0.1	0.2416	0.2
100.0	1.0	0.2380	2.0

TABLE III. Parameters  $\lambda$ ,  $A$ , and  $K$  (divided by  $N$ ) at which simulations were carried out for the  $N = 8$  chiral  $\phi^4$  model. Physical quantities were observed for every  $C_{INT} \times L^2$  MCS.